Chemical Science

ROYAL SOCIETY OF CHEMISTRY

EDGE ARTICLE

View Article Online
View Journal

Cite this: DOI: 10.1039/d5sc08291a

All publication charges for this article have been paid for by the Royal Society of Chemistry

Heterometallic ion-regulated full-color gold nanoclusters for multicolor bioimaging and circularly polarized luminescence

Yaguang Yin,† Gan Zhao,† Fanfan Yu† and Honglin Liu *

Received 27th October 2025
Accepted 7th November 2025

DOI: 10.1039/d5sc08291a

rsc.li/chemical-science

Achieving tunable full-color emission and high-efficiency circularly polarized luminescence (CPL) from a single type of nanocluster remains a major challenge due to weak dissymmetry factors and aggregation-induced quenching. This study reports a breakthrough synthesis of full-color-emitting gold nanoclusters *via* heterometallic ion doping. By reducing $HAuCl_4$ with 4-amino-2-mercaptopyrimidine (AMP) in the presence of Cr^{3+}, Mg^{2+}, or Ag^{+}, blue (400 nm), green (495 nm), and red (700 nm) emissive NCs were obtained with respective quantum yields of 13.2%, 2.46%, and 3.34%. Structural analysis confirmed compositions of $Au_7(AMP)_5Cr_2$, $Au_6(AMP)_4Mg_2$, and $Au_6(AMP)_3Ag$, all <1.1 nm. Density functional theory calculations further reveal that b-NCs, g-NCs and r-NCs regulate emission energy through local coordination, electronic coupling, and structural rigidity of the Au(I)–SR framework. In summary, dopant ions serve as cross-linkers in surface Au(I)–thiolate motifs, with motif length determining emission color. Co-assembly with chiral lipid gelators induced full-color CPL ($g_{lum} = 10^{-2}$) *via* structural rigidification within helical nanotubes. The NCs showed low cytotoxicity and enabled multicolor bioimaging. Anti-counterfeiting gels with dual-level encryption were developed using UV-triggered fluorescence and CPL-handedness. The materials remained stable over one month. This work establishes a metal-ion-directed strategy for emission tuning in Au NCs, linking structures to photophysical properties and offering a flexible platform for chiral optoelectronics.

Introduction

Metal nanoclusters (NCs), comprising a few to tens of atoms with sizes near the electron Fermi wavelength, bridge the gap between atomic and nanoparticle behaviors in chirality,[1] catalysis,[2] electrochemistry[3] and magnetism,[4] exhibiting discrete electronic transitions and molecule-like photoluminescence (PL).[5] Their ultrasmall dimensions, low toxicity, biocompatibility, and photostability surpass those of traditional fluorophores (*e.g.*, organic dyes and quantum dots),[6,7] enabling transformative applications in biosensing, bioimaging, and theranostics. However, most NCs emit at a single wavelength, severely limiting their utility in multiplexed detection, full-color displays, and advanced optical encoding. Achieving tunable, continuous full-color emission from a single NC system remains a fundamental challenge. Concurrently, imparting circularly polarized luminescence (CPL) crucial for 3D displays, encrypted storage, and chiral optoelectronics to NCs typically relies on intrinsically chiral nanostructures or chiral ligand capping, which suffer from limited generality, quantum efficiency losses, and aggregation-induced quenching. Integrating full-color tunability with high-performance CPL in a unified platform represents a significant unmet goal in nanophotonic materials.

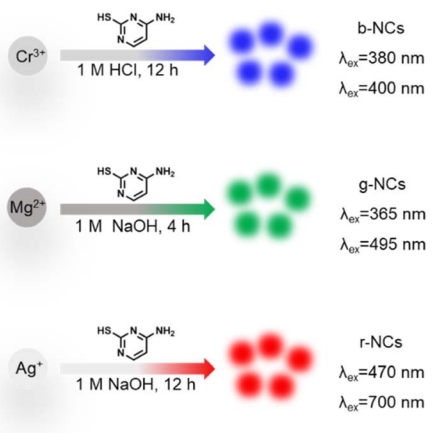

Scheme 1 Schematic illustration of the one-pot synthesis strategy for heterometallic ion-regulated full-color Au NCs.

Joint Research Center for Food Derived Functional Factors and Synthetic Biology of IHM, Anhui Provincial International Science and Technology Cooperation Base for Major Metabolic Diseases and Nutritional Interventions, China Light Industry Key Laboratory of Meat Microbial Control and Utilization, School of Food and Biological Engineering, Engineering Research Center of Bio-process, Ministry of Education, Hefei University of Technology, Hefei 230601, P. R. China. E-mail: liuhonglin@mail.ustc.edu.cn; liuhonglin@hfut.edu.cn

† Yaguang Yin, Gan Zhao and Fanfan Yu contributed equally to this work.

Significant efforts have been devoted to modulating NC emission. Strategies include surface ligand engineering (altering electronic states),[8,9] kernel alloying (modifying metal composition/electronic structure),[10] aggregation-induced emission (AIE),[11] self-assembly,[12] and environmental manipulation.[13] Alloying,[14] in particular, *via* co-reduction,[15] galvanic exchange,[16] ligand-induced conversion,[17] or intercluster reactions,[18] can shift emission wavelengths.[19] For instance, Ag_{25} templates enable the synthesis of center-doped $[M@Ag_{24}]$ clusters (M = Ni, Pd, Pt) by the galvanic exchange strategy,[16] while the intercluster reaction of $[Au_{25}(PET)_{18}]^-$ and $[Ag_{25}(DMBT)_{18}]^-$ clusters yields adducts like $[Au_{25}Ag_{25}(PET)_{18}(DMBT)_{18}]^{2-}$.[18] However, these approaches offer only discontinuous or narrowly continuous (<100 nm) spectral shifts and often involve complex multi-step syntheses. Crucially, achieving continuous, wide-range visible full-color emission from a single type of parent cluster using a unified synthesis strategy remains elusive, hindered by insufficient understanding of the structural motifs dictating emission energy and the lack of precise control methods.

Chirality underpins biological function and advanced materials.[20] Materials exhibiting CPL-emitting left-handed or right-handed circularly polarized light-hold immense promise for next-generation technologies like 3D displays,[21] secure information storage,[22] biological coding,[23] and chiral optoelectronic devices.[24] CPL in NCs typically arises through three mechanisms: (1) intrinsic chirality from asymmetric defects,[25] (2) ligand-induced chirality *via* chiral capping agents,[26] or (3) chirality transfer from chiral matrices.[27] While chiral ligand capping is common,[28] it is restricted by rare ligand choice, often yields weak signals with a luminescence dissymmetry factor (g_{lum}) of about 10^{-5}–10^{-3}, and faces challenges in achieving high quantum yields due to aggregation-caused quenching (ACQ). Full-color CPL materials, capable of encoding information across wavelengths, are exceptionally rare due to synthetic complexity and the difficulty in simultaneously controlling emission color, intensity, and dissymmetry.[29] The development of simple, versatile strategies to induce robust, full-color CPL in highly emissive, achiral NCs is thus critically needed.

Herein, we report a strategy for synthesizing full-color-emitting gold nanoclusters (Au NCs) *via* heterometallic ion doping and demonstrate their conversion into full-color CPL-active materials through co-assembly with chiral gels. The key innovation lies in the discovery that dopant ions (Cr^{3+}, Mg^{2+}, and Ag^+) function as cross-linkers, modulating the length of surface Au(I)–thiolate motifs that directly determine the emission wavelength: longer motifs yield higher-energy (blue) emission, whereas shorter motifs produce lower-energy (red) emission. This mechanism enables continuously tunable photoluminescence spanning the entire visible range (400–700 nm) from a single NC synthesis system using a unified one-pot approach (Scheme 1). Importantly, combined structural analyses and theoretical calculations established a clear structure–emission correlation, elucidating how local coordination and electronic coupling dictate the emission behavior. Furthermore, we developed a versatile "host–guest" co-assembly strategy, in which these achiral, full-color Au NCs are integrated with chiral lipid gelators to induce efficient chirality transfer. This process generates mirror-image CPL signals across the visible spectrum through structural rigidification within helical nanotubes. The integration of full-color tunability, efficient CPL generation, low cytotoxicity, and excellent stability enables innovative multi-level anti-counterfeiting applications based on fluorescence color and CPL handedness. This work not only provides fundamental insights into the emission mechanisms of Au NCs but also offers a robust platform for designing next-generation multifunctional chiral optoelectronic materials.

Results and discussion

One-pot synthetic heterometallic ion-doped gold nanoclusters with full-color-tunable emission

Novel heterometallic ion-doped full-color Au NCs were synthesized *via* a facile one-pot reduction of $HAuCl_4$ with 4-amino-2-mercaptopyrimidine (AMP) ligands in the presence of Cr^{3+}, Mg^{2+}, or Ag^+ cations. Comprehensive optical characterization revealed distinct photophysical properties for each NC type. As shown in Fig. 1a, all three NC solutions exhibited symmetric, single-peak emission spectra centered at 400 nm (blue, b-NCs), 495 nm (green, g-NCs), and 700 nm (red, r-NCs), spanning the visible to near-infrared spectrum. Corresponding optimal excitation wavelengths were 380 nm, 365 nm, and 470 nm, respectively. Bright blue, green, and red emissions under UV illumination (inset, Fig. 1a) aligned with Commission Internationale de l'Eclairage (CIE) chromaticity coordinates progressing from blue to red (Fig. 1b inset). Absolute PL quantum yields (QYs) were determined to be 13.2% (b-NCs), 2.46% (g-NCs), and 3.34% (r-NCs) (Fig. 1b). UV-vis absorption spectra (Fig. 1c) displayed characteristic features of ultrasmall NCs: strong sub-300 nm peaks (b-NCs: 233/265 nm; g-NCs: 240/273 nm; r-NCs: 207/235/290 nm) with significant shifts *versus* free AMP ligands (240/270 nm, Fig. S1), confirming Au-ligand complex formation. All samples showed monotonically decreasing absorption tails beyond 300 nm a hallmark of few-atom nanoclusters.[31] Time-resolved PL decay profiles (Fig. 1d and Table 1) yielded average lifetimes of 4.81 μs (b-NCs), 4.99 μs (g-NCs), and 6.73 μs (r-NCs), fitted with bi-/tri-exponential functions. Crucially, excitation–emission contour maps (Fig. 1e) demonstrated fixed emission maxima regardless of the excitation wavelength, while single excitation bands and emission peaks (Fig. 1a) confirmed homogeneous emissive species in each sample.

Furthermore, control experiments were conducted to verify the origin of the PL. The results clearly demonstrate that the characteristic excitation–emission pairs-approximately 380 → 400 nm for b-NCs, 365 → 495 nm for g-NCs, and 470 → 700 nm for r-NCs-are only observed in the complete systems comprising Au, AMP, and the corresponding heterometal ions (Cr^{3+}, Mg^{2+}, or Ag^+). By contrast, neither pure AMP ligands nor synthetic intermediates lacking the critical metal ions produced any detectable emission under identical excitation conditions (Fig. S2). This absence of luminescence in incomplete assemblies underscores the essential role of the integrated metal–ligand architecture in generating the observed optical signals. It

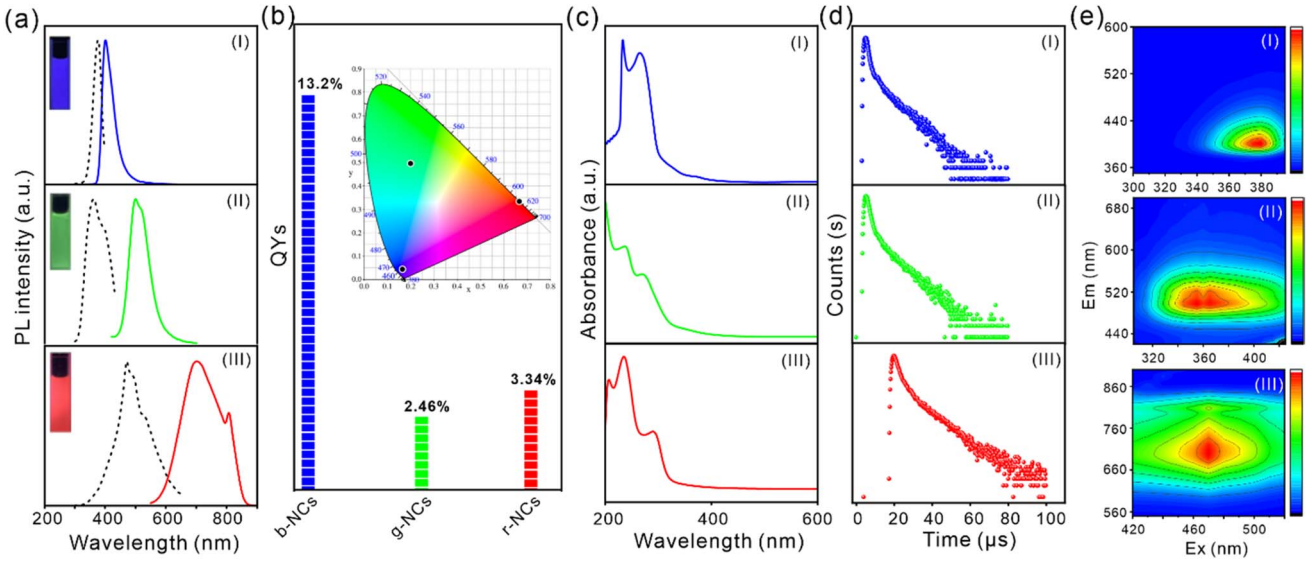

Fig. 1 Optical properties of full-color Au NCs. (a) Emission (solid lines) and excitation spectra (dotted lines). Insets: photographs under UV light (365 nm). (b) Absolute PL quantum yields. Insets: chromaticity coordinates. (c) UV-vis absorption spectra. (d) Time-resolved PL decay curves. (e) Excitation–emission contour mapping. Note: (I) b-NCs, (II) g-NCs and (III) r-NCs.

is noteworthy that the apparent mismatch between the excitation–emission wavelengths and the dominant absorption peaks aligns with behavior documented in previous studies of luminescent metal nanoclusters.[11,30] In such systems, the emissive states frequently arise from weak electronic transitions appearing as shoulders or tails in the absorption spectrum, rather than from the stronger, ligand-centered absorption bands that typically dominate the main peak. This phenomenon is often attributed to the fact that the dominant absorption bands are typically associated with high-energy, ligand-centered transitions, whereas the emission originates from lower-energy states influenced by metal–ligand coordination or charge-transfer processes. Collectively, these control experiments and spectral analyses confirm that the luminescence originates from the well-defined electronic structure of the metal–ligand clusters themselves, rather than from impurities or free ligands. Therefore, the b-NCs, g-NCs, and r-NCs can be regarded as high-purity, monodisperse luminescent entities possessing intrinsic and well-defined optical characteristics.

Metal ion-mediated luminescence mechanism for emission regulation

Comprehensive structural characterization revealed the mechanism underlying metal-ion-mediated emission tuning. Electrospray ionization mass spectrometry (ESI-MS) confirmed NC compositions: $m/z = 2156$ for b-NCs $[Au_7(AMP)_5Cr_2]$, $m/z = 1741$ for g-NCs $[Au_6(AMP)_4Mg_2]$, and $m/z = 1691$ for r-NCs $[Au_6(AMP)_3Ag]$ (Fig. 2a–c and S3–S5). Transmission electron microscopy (TEM) revealed ultrasmall spherical particles (0.93 ± 0.19 nm for b-NCs, 0.95 ± 0.15 nm for g-NCs, and 1.10 ± 0.20 nm for r-NCs) with narrow size distributions (Fig. 2d–f), consistent with their compositions.[32] X-ray photoelectron spectroscopy (XPS) analysis revealed a pronounced evolution in the oxidation states of gold. The Au(0)/Au(I) ratio systematically increased from 1 : 6 in the b-NCs to 2 : 4 in the g-NCs and further to 5 : 1 in the r-NCs. This trend corresponds to a progressive decrease in the fractional content of Au(I) from 85.7% to 66.7% and finally to 16.7%. The observed reduction in Au(I) content exhibits a strong correlation with the red-shift in the PL emission (Fig. 2g–i), indicating a direct link between the structure of the nanoclusters and their optical properties.

Fourier-transform infrared (FTIR) spectroscopy provided compelling evidence of metal–ligand coordination and electronic redistribution during the formation of the heterometallic nanoclusters. Comparative analysis of the spectra for pure AMP, the Au-free intermediate, the metal-free (M-free) intermediate, and the three final nanoclusters (b-NCs, g-NCs, and r-NCs) revealed systematic vibrational shifts (Fig. S6). Specifically, the C–N stretching vibration exhibited a distinct blue shift-from

Table 1 Fluorescence lifetime of AMP-Au NC

Species	Chemical formula	Au(0)/Au(I)	Sizes/nm	λ_{ex} [nm]	λ_{em} [nm]	B_1 [%]	τ_1 [μs]	B_2 [%]	τ_2 [μs]	τ_{avg} [μs]	χ^2
b-NCs	$Au_7(C_4H_4N_3S)_5Cr_2$	1/6	0.93 ± 0.19	380	400	53.00	1.24	47.00	8.84	4.81	1.26
g-NCs	$Au_6(C_4H_4N_3S)_4Mg_2$	2/4	0.95 ± 0.15	365	495	54.73	1.90	45.27	8.74	4.99	1.20
r-NCs	$Au_6(C_4H_4N_3S)_3Ag$	5/1	1.10 ± 0.20	470	700	48.86	2.30	51.14	10.97	6.73	1.28

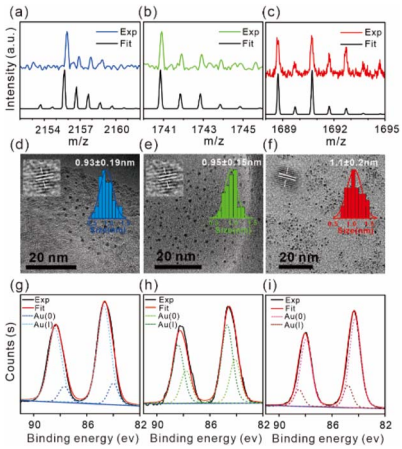

Fig. 2 Structural properties of full-color Au NCs. Experimental (colored line) and calculated (black line) ESI-MS spectra of (a) b-NCs, (b) g-NCs and (c) r-NCs, respectively. TEM images of (d) b-NCs, (e) g-NCs and (f) r-NCs, respectively. XPS spectra with fitting results for (g) b-NCs, (h) g-NCs and (i) r-NCs, respectively.

1298 cm^{-1} in pure AMP to 1312–1357 cm^{-1} in the nanoclusters-indicating bond strengthening and charge redistribution induced by coordination. The C=C and C=N stretching vibrations displayed dopant-dependent behavior. In the presence of Cr^{3+} or Mg^{2+} ions, which possess electron-withdrawing characteristics, these bands shifted slightly to higher wavenumbers. In contrast, Ag^{+} doping, known for its strong electron back-donation capability, caused pronounced red shifts.[33] Additionally, the N–H vibration shifted from its original position to approximately 1640–1650 cm^{-1} upon cluster formation. Importantly, new absorption bands emerged in the 1720–1790 cm^{-1} region, which were absent in all control samples (pure AMP, Au-free, and M-free), signifying substantial electronic rearrangements of the ligands associated with the formation of coordinated structures.[34] Further FTIR analysis (Fig. S7) confirmed the coordination mode of the AMP ligand to the gold core. The appearance of a band at 2977 cm^{-1}, assigned to C=C–H deformation, indicates successful formation of Au–S bonds. Meanwhile, the disappearance of the N–H stretching vibration at 3103 cm^{-1} provides strong evidence of Au–N coordination, confirming a multidentate binding geometry.

We also examined the effect of solvent and temperature on the PL to elucidate how environmental rigidity complements the metal-ion-directed emission mechanism. The PL spectra of purified NCs dispersed in 2-propanol (IPA)/H_2O mixtures (varying volume fraction $f_{organic} = V_{IPA}/(V_{IPA} + V_{H_2O})$) revealed a critical trend: PL intensities of all NCs (b-NCs, g-NCs, and r-NCs) increased progressively with higher f_{IPA} (Fig. 3a–f). This enhancement correlates with the elevated viscosity of IPA (coefficient ~1.8 cP *vs.* H_2O ~0.8 cP, 30 °C), which restricts intramolecular rotation/vibration of the AMP ligands. Consequently, non-radiative relaxation pathways are suppressed, favoring radiative decay-a phenomenon consistent with the metal-ion-induced rigidification of surface motifs.[35] Temperature-dependent studies further validated this rigidity-PL relationship: cooling samples from 298 K to 77 K markedly enhanced PL intensity for all NCs (Fig. 3g–i). At cryogenic temperatures, the ligand shell undergoes rigidification, immobilizing surface motifs and minimizing vibrational/rotational energy dissipation.[36,37] These findings demonstrate that solvent polarity and thermal energy modulate PL efficiency by tuning molecular mobility, while heterometallic ions (Cr^{3+}, Mg^{2+}, and Ag^{+}) primarily dictate the emission wavelength

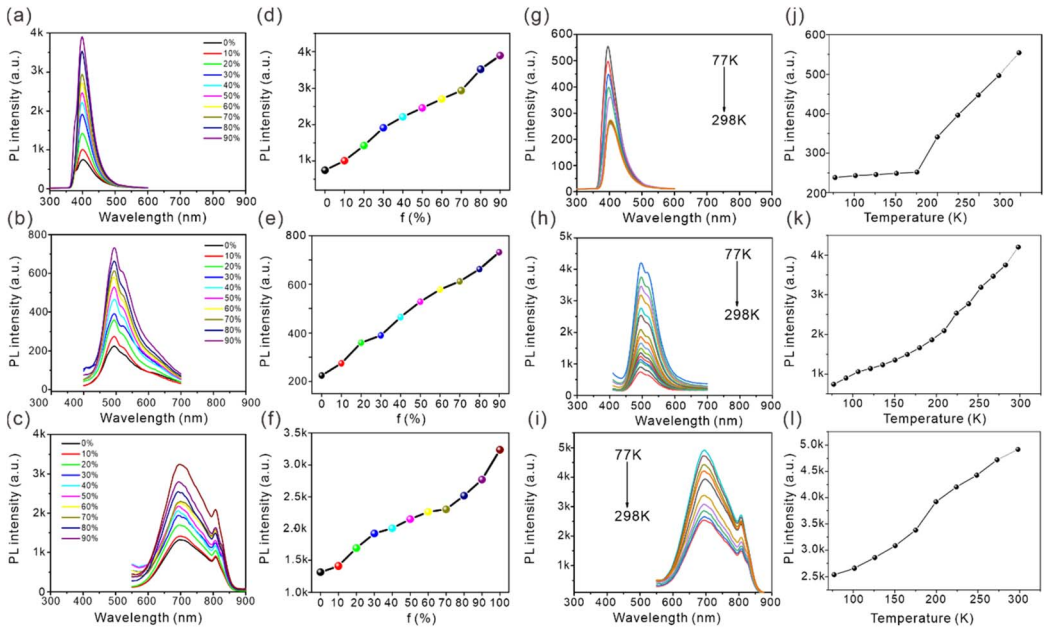

Fig. 3 Solvent- and temperature-dependent fluorescence enhancement of heterometallic Au NCs. Fluorescence spectra of (a) b-NCs, (b) g-NCs and (c) r-NCs in different solvent systems, (d) b-NC, (e) g-NC and (f) r-NC fluorescence trends in different solvent systems, (g) b-NCs, (h) g-NCs and (i) r-NCs at low temperature, and (j) b-NC, (k) g-NC and (l) r-NC fluorescence trends at different temperatures.

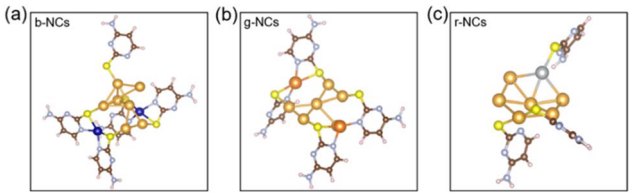

Fig. 4 DFT-optimized structures of heterometal-doped Au NCs. (a) b-NCs; (b) g-NCs; (c) r-NCs.

through motif-length control-highlighting a synergistic hierarchy in optical regulation.

To elucidate the intrinsic mechanism underlying the tunable PL of heterometal-doped nanoclusters, we performed DFT calculations based on the comprehensive experimental data obtained.[38] For the b-NCs (Fig. 4a), geometry optimization revealed that each Cr^{3+} center forms two short Cr–S bonds (2.38–2.41 Å), effectively bridging adjacent Au–SR motifs. Concurrently, the sulfur atoms remain bonded to neighboring Au atoms (Au–S = 2.44–2.47 Å), collectively forming a distinct dual-anchored bridge structure. The short nearest Cr–Au distances (2.90–3.10 Å, Table S4) indicate that the Cr^{3+} ions reside on the cluster surface and exhibit significant electronic coupling with the gold core. The calculated HOMO–LUMO energy gap is 2.942 eV, which is consistent with the observed high-energy blue emission. The incorporation of Cr^{3+} shifts the low-lying unoccupied molecular orbitals to the Cr-d manifold, thereby widening the fundamental energy gap and enhancing the structural rigidity of the Au–SR network. These combined effects account for the blue-shifted and intensified luminescence. Regarding the g-NCs (Fig. 4b), the optimized geometry indicates that Mg^{2+} primarily coordinates to the nitrogen atoms of the AMP ligands (Mg–N ≈ 2.20 Å), while maintaining longer, non-bonded contacts with sulfur atoms (2.64–2.72 Å, Table S5). Due to the absence of low-lying d orbitals, Mg^{2+} contributes minimally to the frontier orbitals directly. Its primary role lies in exerting electrostatic polarization and imposing local geometric constraints, which collectively modulate the electronic distribution within the Au–S motifs. Consequently, the HOMO–LUMO gap decreases to 2.618 eV, corresponding to emission in the green region. This reduction in the energy gap arises from enhanced electronic coupling and a slight relaxation of the structural rigidity. Furthermore, the electrostatic field introduced by Mg^{2+} can influence non-radiative decay pathways, thereby indirectly modulating the emission efficiency. For the r-NCs (Fig. 4c), the DFT-optimized structure shows that Ag^{+} is located on the surface, directly coordinated to sulfur (Ag–S ≈ 2.42 Å), and exhibits short Ag···Au contacts (2.78–2.84 Å) with nearby gold atoms (Table S6). The closed-shell d^{10} configuration of Ag^{+} precludes direct contribution to low-lying orbitals; however, its surface coordination and the resulting near-field polarization effectively strengthen the Au–Au and Au–S electronic interactions. This leads to a further reduction of the HOMO–LUMO gap to 2.416 eV. This narrowed energy gap is responsible for the red-shifted emission, originating from enhanced surface polarization and increased electron delocalization among the gold atoms. Critically, control experiments confirmed the absence of detectable PL in the absence of heterometal dopants (Fig. S8). This unequivocally demonstrates that the observed emission and its spectral tunability originate from the heterometal-induced modulation of the Au–SR motifs, rather than from intrinsic Au–ligand interactions. In summary, although the b-NCs, g-NCs, and r-NCs exhibit markedly different coordination modes with their respective heterometal ions, they all regulate the emission energy by strategically altering the local coordination environment, electronic coupling, and structural rigidity of the Au(I)–SR framework.

In contrast to conventional strategies for achieving multicolor emission in Au NCs-which often rely on varying reducing agents and reaction conditions to precisely control cluster size-our work introduces a distinct approach.[39] We utilize heterometal ions (Cr^{3+}, Mg^{2+}, and Ag^{+}) as structural cross-linkers in a facile one-pot aqueous synthesis. These cross-linkers directly regulate the length of the surface Au(I)–thiolate motifs, thereby enabling tunable full-color PL across the visible spectrum (400–700 nm). This method not only significantly simplifies the synthetic procedure but also allows for more predictable control over the emission color. Regarding the underlying mechanism, we establish a clear structure–property relationship: extended Au(I)–SR motifs, facilitated by Cr^{3+} doping, strengthen the Au(I)–Au(I) coupling, resulting in higher-energy blue emission. Conversely, fragmented motifs, induced by Ag^{+} doping, weaken this coupling, leading to lower-energy red emission. This proposed mechanism is robustly supported by multiple lines of evidence. XPS analysis reveals a systematic decrease in the Au(I)/Au(0) ratio from 6 : 1 to 1 : 5 across the series. Furthermore, solvent- and temperature-dependent PL studies confirm the crucial role of motif rigidity in determining the luminescence properties. DFT calculations provide additional atomic-level insight, indicating that despite their distinct coordination geometries, the b-NCs, g-NCs and r-NCs uniformly modulate their emission energy by fine-tuning the local coordination environment, electronic coupling, and structural rigidity of the Au(I)–SR framework. In summary, our findings reveal that the introduced heterometal dopants (Cr^{3+}, Mg^{2+}, and Ag^{+}) act as cross-linking centers that dictate the effective length of the surface Au(I)–thiolate motifs. This motif length, in turn, directly governs the emission wavelength, with longer motifs corresponding to higher-energy (blue) emission and shorter motifs corresponding to lower-energy (red) emission.

Biocompatibility and multicolor cellular imaging performance of full-color Au NCs

Given their exceptional luminescent properties, we evaluated the biomedical potential of full-color Au NCs by assessing biocompatibility and cellular imaging performance in HeLa cells. Cytotoxicity analysis *via* Annexin V-FITC/PI staining and flow cytometry revealed negligible apoptosis/necrosis induction after 24 h of incubation with 100 μg per mL NCs (b-NCs, g-NCs, or r-NCs). As shown in Fig. S9a–d, cell viability distributions across quadrants (I: viable, II: early apoptotic, III: late apoptotic, and IV: necrotic) remained comparable to those of untreated controls (Fig. S9i).

To assess oxidative stress, intracellular reactive oxygen species (ROS) generation was quantified using DCFH-DA fluorescence. Flow cytometry (Fig. S9f–h and j) confirmed that minimal ROS induction-signals from NC-treated cells were only marginally higher than those from negative controls and substantially lower than those from H_2O_2-treated positive controls. This demonstrates the Au NC biocompatibility and lack of oxidative damage.

For cellular imaging, HeLa cells incubated with 50 μg per mL NCs for 2 h exhibited intense cytoplasmic fluorescence: blue (b-NCs), green (g-NCs), and red (r-NCs) emissions localized exclusively in the cytoplasm (Fig. S9k–m). Bright-field images confirmed preserved cell morphology after 24 h of exposure (Fig. S9n), validating low cytotoxicity. These results establish that the full-color Au NCs combine low cytotoxicity, minimal ROS generation, efficient cellular uptake, and bright organelle-specific emission, positioning them as superior multiplexed bioimaging probes for real-time subcellular tracking.

Full-color circularly polarized luminescence *via* chiral co-assembly of Au NCs with lipid gelators

Here, the synthesized Au NCs are ideally suited for constructing multicolor CPL materials owing to their tunable emission colors, superior optical properties, and straightforward synthesis. We designed a "chiral host-luminescent guest" composite system by embedding achiral Au NCs within chiral lipid gelators (LGAm and its enantiomer DGAm), which self-assemble into uniform helical nanotubes (Fig. S10), providing chiral microenvironments for NC immobilization. Co-assembled gels were prepared by mixing LGAm/DGAm with b-NCs, g-NCs, or r-NCs in selective solvents. Circular dichroism (CD) spectroscopy confirmed that the ground-state chirality of the co-gels matched that of pure LGAm/DGAm (Fig. S11), though co-assembly-induced CD signals were obscured by strong gel scattering. The CPL generation mechanism involves chirality transfer through rigidification: strong host–guest interactions (electrostatic/hydrogen bonding) immobilize NCs on chiral nanotube surfaces, suppressing ligand vibration/rotation and populating radiative decay pathways. This was validated by the absence of CPL in disintegrated THF solutions of b-NCs/DGAm mixtures (Fig. 5a and S12), despite intense blue emission-demonstrating that nanotube confinement is essential for inducing excited-state chirality.

To confirm successful NC incorporation into the gel matrix, we analyzed PL spectra of the co-assemblies (Fig. S13). Under UV excitation, all gel composites exhibited intense emissions spanning 400–800 nm, with distinct peaks at 420 nm (LGAm/b-NCs), 520 nm (LGAm/g-NCs), and 720 nm (LGAm/r-NCs). Notably, these emissions displayed significant redshifts of 20 nm (b-NCs), 25 nm (g-NCs), and 20 nm (r-NCs) compared to their solution-state counterparts, indicating surface motif reorganization upon confinement within the chiral nanotubular framework. Morphological characterization revealed that pure LGAm gels formed uniform nanotubes (Fig. S10).[40] Remarkably, co-assembly with NCs (exemplified by LGAm/b-NCs) preserved this nanotubular architecture without

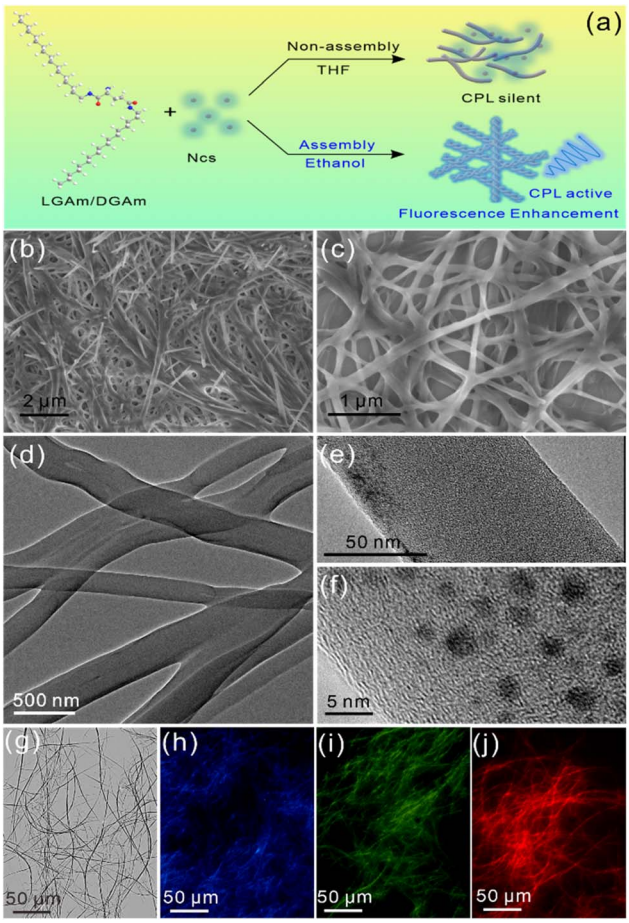

Fig. 5 Morphological and mechanistic characterization of chiral co-assembled gels embedded with Au NCs. (a) Proposed CPL generation mechanism. (b and c) SEM images of LGAm/b-NCs gels at different magnifications. (d–f) High-resolution TEM images showing b-NCs uniformly decorating nanotube surfaces without aggregation. (g) Optical microscopy image of LGAm/b-NCs gels exhibiting fibrous morphology. Fluorescence microscopy images of (h) LGAm/b-NCs, (i) LGAm/g-NCs and (j) LGAm/r-NCs gels.

structural disruption, as evidenced by SEM (Fig. 5b–d). High-resolution TEM further confirmed that b-NCs densely decorated nanotube surfaces while retaining their individual morphology (Fig. 5e and f), demonstrating effective "host–guest" integration without aggregation-induced distortion. FTIR spectra showed that the amide I and amide II bands at around 1633 cm^{-1} and 1530 cm^{-1} were still stable in LGAm/b-NCs compared with pure LGAm (Fig. S14), and the all-trans-configuration arranged alkyl chains showed asymmetric and symmetric CH_2 stretching vibrations at 2919 and 2851 cm^{-1}, respectively, which indicated that the addition of b-NCs did not affect the formation of the gel, let alone destroy the structure of the gel. Another interesting finding is that the $-NH_2$ bending vibration of LGAm at 1472 cm^{-1} was slightly red shifted to 1468 cm^{-1} due to electrostatic interaction. Meanwhile, after the formation of LGAm/b-NCs, the –OH stretching vibration peak at 3200 cm^{-1} was replaced by the N–H stretching vibration of the amino and amide groups in the form of hydrogen bonding at

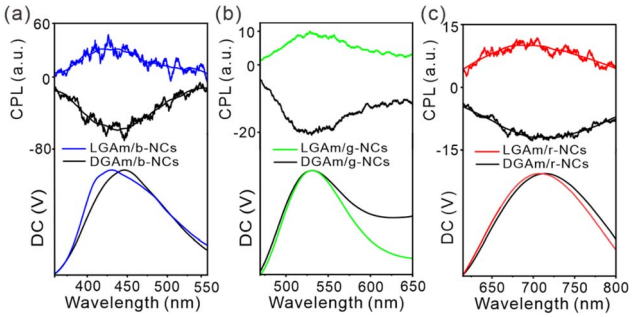

Fig. 6 Full-color CPL and unpolarized fluorescence of Au NCs co-assembled with chiral lipid gelators. (a) LGAm (DGAm)/b-NCs, (b) LGAm (DGAm)/g-NCs and (c) LGAm (DGAm)/r-NCs.

3324 cm^{-1}, and the stretching vibration peak of the free –OH was observed near 3674 cm^{-1}, while the N–H stretching vibration peak of LGAm/b-NCs was slightly red shifted compared with that of LGAm. The above results clearly indicate that electrostatic interactions and hydrogen bond formation may be the key to induce NCs and gel co-assembly to form CPLs. Optical and fluorescence microscopy images of the panchromatic LGAm/NCs are shown in Fig. 5g–j. All the NC-doped gels presented long micrometer fiber structures with similar morphology, and the co-assemblies displayed bright fluorescence and multiple emission colors. These observations suggested that host nanotubes had strong capacity to integrate the extraneous guest NCs, and NCs of various luminescent colors could form "host–guest" interactions with the gels, leading to multicolor emission assemblies.

Remarkably, the co-assembled gels exhibited pronounced excited-state chirality, generating strong mirror-image CPL signals across the entire visible spectrum (350–800 nm) for all three emission colors (Fig. 6). Specifically, DGAm-based gels (embedded with b-NCs, g-NCs, or r-NCs) displayed negative CPL peaks (left-handed), while LGAm-based counterparts showed positive peaks (right-handed). The unpolarized fluorescence (DC) spectra aligned precisely with CPL emission maxima, confirming that the circularly polarized emission originated from the same electronic transitions. The luminescence dissymmetry factor (glum), quantifying CPL intensity asymmetry, was calculated as

$$g_{lum} = 2\frac{I_L + I_R}{I_L - I_R}$$

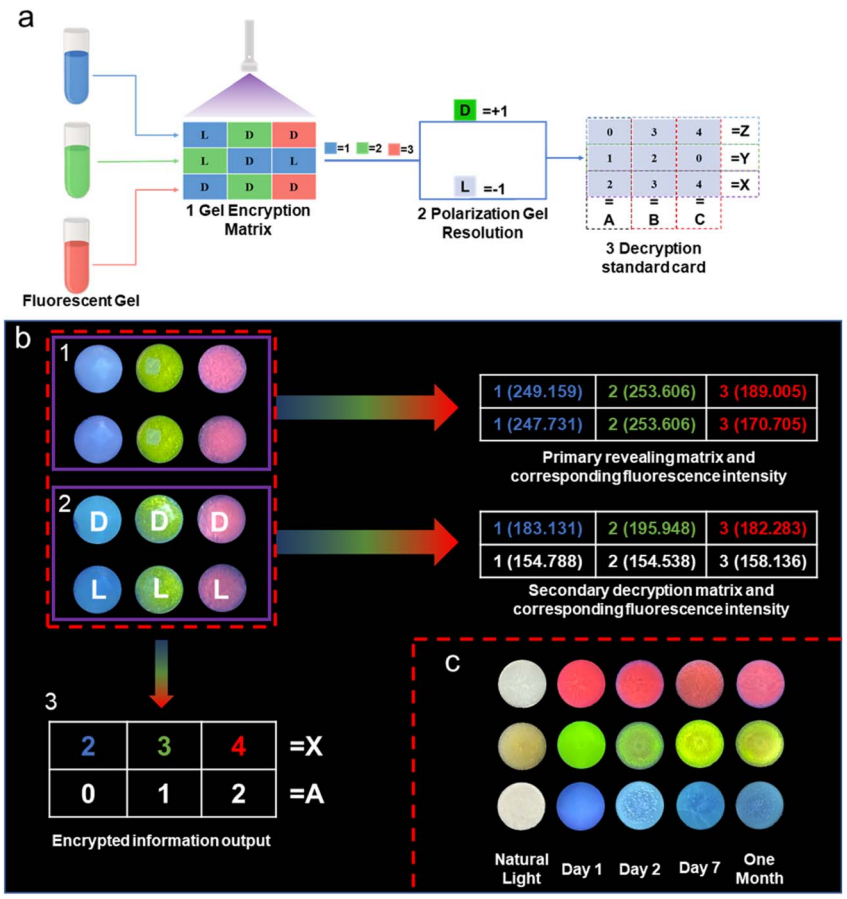

Fig. 7 Dual-level anti-counterfeiting films based on full-color CPL. (a) Encryption mechanism schematic: integration of fluorescence color coding (primary) and CPL handedness verification (secondary) for high-security authentication. (b) (1) UV-excited fluorescence (365 nm) of gel films: blue (b-NCs), green (g-NCs), and red (r-NCs) with assigned codes (1–3). (2) CPL-handedness identification under a polarized filter: left-CPL (–1, blue matrix); right-CPL (+1, red matrix). (3) Decrypted messages "X" and "A" *via* cross-referencing the dual-code matrix. (c) Stability validation: unchanged fluorescence after 1-month ambient storage.

where I_L and I_R represent left-handed and right-handed CPL intensities, respectively. Experimentally, g_{lum} was derived from ellipticity measurements:

$$g_{lum} = 2 \times [\text{ellipticity}/(32\,980/\ln 10)]/\text{total fluorescence intensity at the CPL extremum.}$$

All co-gels achieved g_{lum} values in the order of 10^{-3} (Fig. S15), with the LGAm/b-NCs system exhibiting the highest dissymmetry ($g_{lum} = -1 \times 10^{-2}$) surpassing or matching that of other composite systems.

New anti-counterfeiting technologies are of great significance to social sustainability, medical health, and market stability.[41] Leveraging their multichannel optical responses, we developed advanced anti-counterfeiting films with dual-level encryption capabilities (Fig. 7a). These chiral luminescent films integrate multiple optical signals-fluorescence and CPL-making them ideal for high-security applications. As a proof of concept, three gel films were engineered to emit blue, green, or red fluorescence under 365 nm UV light (Fig. 6b1). There are two layers of encryption mechanism. Primary encryption (fluorescence coding): each color was assigned a digital code: blue = 1, green = 2, and red = 3, forming a first-level encryption matrix. Secondary encryption (CPL handedness): using a quarter-wave plate and linear polarizer, films exhibiting left-handed CPL were coded as −1, while right-handed CPL as +1 (Fig. 7b2). The encrypted message "X" and "A" was decoded by cross-referencing the numerical matrix with the standard key in Fig. 7a (Fig. 7b3). Crucially, insertion of a polarizing filter caused marked intensity reduction (Fig. 7b1 *vs.* 7b2), demonstrating that part of the fraction of the luminescence arises from circularly polarized emission rather than from residual unpolarized fluorescence, which likely originates from loosely bound clusters in the gel matrix. The gel film demonstrates excellent long-term stability, as evidenced by its nearly unchanged fluorescence intensity after being stored under ambient conditions for one month (Fig. 7c). This remarkable durability originates from strong electrostatic and hydrogen-bonding interactions that effectively anchor the Au NCs within the confined spaces of the self-assembled helical nanotubes. This configuration not only shields the Au NCs from oxidative degradation but also suppresses non-radiative decay pathways. Furthermore, the dynamic hydrophobic domains formed by the alkyl chains contribute to stress dissipation, which ensures the material's mechanical flexibility. Owing to this synergistic design, the gel film achieves robust, full-color CPL emission and enables dual-layer encryption functionality, thereby showcasing significant potential for advanced security applications.

In contrast to previous strategies for generating CPL, which often rely on rigid liquid-crystal templates requiring elaborate dual-ligand engineering, our work introduces a distinct and simplified approach based on a flexible hydrogel assembly. Within this system, chiral lipid nanotubes (LGAm/DGAm) spontaneously encapsulate Au NCs through synergistic hydrogen-bonding and electrostatic interactions, enabling highly efficient chirality transfer without the need for complex ligand modifications. Moreover, whereas earlier studies were typically limited to demonstrating a single CPL emission band in the near-infrared region (*e.g.*, at around 880 nm),[42] our heterometal-ion doping strategy (utilizing Cr^{3+}, Mg^{2+}, and Ag^{+}) achieves broadly tunable, full-color CPL emission across the entire visible spectrum (400–700 nm). This wide-ranging tunability is accomplished by precisely modulating the effective length of the surface Au(I)–thiolate motifs. Going beyond emission tuning, we have further developed innovative dual-level encrypted gel films. These films integrate straightforward fluorescence color codes with the more secure, handedness-dependent CPL signatures to enable dynamic anti-counterfeiting. Notably, these films exhibit remarkable environmental stability, maintaining their performance for over one month under ambient conditions, thereby offering a versatile and robust platform for advanced chiral photonic applications.

Conclusions

In summary, this work demonstrates a general and efficient strategy to achieve tunable full-color luminescence and circularly polarized light emission from a single class of gold nanoclusters (Au NCs). By introducing heterometal ions (Cr^{3+}, Mg^{2+}, and Ag^{+}) as structural cross-linkers, we precisely modulated the emission wavelengths of Au NCs across the visible to near-infrared region (400–700 nm) through controlled variation of the surface Au(I)–thiolate motif length. Structural characterization confirmed the cluster composition and nanoscale dimensions, while DFT calculations revealed that the blue-, green-, and red-emissive NCs modulate their emission energies through distinct local coordination environments, electronic coupling strengths, and structural rigidity within the Au(I)–SR framework. We therefore propose that the dopant ions act as interfacial cross-linkers within the Au(I)–thiolate motifs, with the motif length serving as the key determinant of emission color. The resulting NCs exhibit excellent biocompatibility and low cytotoxicity, enabling their direct use in multicolor bioimaging. Furthermore, by embedding these non-chiral luminescent NCs into chiral, nonfluorescent organogels (DGAm/LGAm) *via* a "host–guest" co-assembly strategy, we fabricated hybrid materials that display strong full-color circularly polarized luminescence (CPL) with outstanding environmental stability. These chiral luminescent gels also enable dual-level optical encryption by integrating emission color with CPL handedness, offering a new paradigm for advanced anti-counterfeiting, information security, and chiroptoelectronic applications. Overall, this study not only elucidates the structural origin of Au NC luminescence but also establishes a versatile, sustainable, and designable platform for next-generation chiral photonic materials and multifunctional optical technologies.

Author contributions

Yaguang Yin: investigation, methodology, formal analysis, data curation, visualization, writing - review & editing. Gan Zhao: investigation, formal analysis, data curation, visualization, writing – original draft. Fanfan Yu: formal analysis, data curation, visualization, writing – review & editing. Honglin Liu:

conceptualization, methodology, formal analysis, data curation, resources, writing – review, editing, and supervision.

Conflicts of interest

The authors declare no competing interests.

Data availability

The data supporting this article have been included as part of the supplementary information (SI). Supplementary information: Details of methods, experimental procedures, and additional data. See DOI: **https://doi.org/10.1039/d5sc08291a**.

Acknowledgements

This work was funded by the Yangtze River Delta Science and Technology Innovation Community Joint Basic Research Project (2024CSJZN1200), the National Natural Science Foundation of China (22474030 and 22274034), and the Fundamental Research Funds for the Central Universities of China (Grant Numbers: PA2023GDGP0040 and PA2024GDGP0037). The authors declare no competing financial interest.

References

1 H. Yang, J. Yan, Y. Wang, G. Deng, H. Su, X. Zhao, C. Xu, B. K. Teo and N. Zheng, From Racemic Metal Nanoparticles to Optically Pure Enantiomers in One Pot, *J. Am. Chem. Soc.*, 2017, **139**(45), 16113–16116.

2 S. Zhao, R. Jin and R. Jin, Opportunities and Challenges in CO_2 Reduction by Gold- and Silver-Based Electrocatalysts: From Bulk Metals to Nanoparticles and Atomically Precise Nanoclusters, *ACS Energy Lett.*, 2018, **3**(2), 452–462.

3 K. Kwak and D. Lee, Electrochemistry of Atomically Precise Metal Nanoclusters, *Acc. Chem. Res.*, 2019, **52**(1), 12–22.

4 M. Agrachev, S. Antonello, T. Dainese, M. Ruzzi, A. Zoleo, E. Apra, N. Govind, A. Fortunelli, L. Sementa and F. Maran, Magnetic Ordering in Gold Nanoclusters, *ACS Omega*, 2017, **2**(6), 2607–2617.

5 I. Chakraborty and T. Pradeep, Atomically Precise Clusters of Noble Metals: Emerging Link between Atoms and Nanoparticles, *Chem. Rev.*, 2017, **117**(12), 8208–8271.

6 J. Xu and L. Shang, Emerging applications of near-infrared fluorescent metal nanoclusters for biological imaging, *Chin. Chem. Lett.*, 2018, **29**(10), 1436–1444.

7 Y. Zheng, L. Lai, W. Liu, H. Jiang and X. Wang, Recent advances in biomedical applications of fluorescent gold nanoclusters, *Adv. Colloid Interface Sci.*, 2017, **242**, 1–16.

8 H. Deng, K. Huang, L. Xiu, W. Sun, Q. Yao, X. Fang, X. Huang, H. A. A. Noreldeen, H. Peng, J. Xie and W. Chen, Bis-Schiff base linkage-triggered highly bright luminescence of gold nanoclusters in aqueous solution at the single-cluster level, *Nat. Commun.*, 2022, **13**(1), 3381.

9 Y. Wang, Z. Liu, A. Mazumder, C. G. Gianopoulos, K. Kirschbaum, L. A. Peteanu and R. Jin, Tailoring Carbon Tails of Ligands on $Au_{52}(SR)_{32}$ Nanoclusters Enhances the Near-Infrared Photoluminescence Quantum Yield from 3.8 to 18.3%, *J. Am. Chem. Soc.*, 2023, **145**(48), 26328–26338.

10 T. Tsukamoto, T. Kambe, A. Nakao, T. Imaoka and K. Yamamoto, Atom-hybridization for synthesis of polymetallic clusters, *Nat. Commun.*, 2018, **9**, 3873.

11 Z. Luo, X. Yuan, Y. Yu, Q. Zhang, D. T. Leong, J. Y. Lee and J. Xie, From Aggregation-Induced Emission of Au(I)-Thiolate Complexes to Ultrabright Au(0)@Au(I)-Thiolate Core-Shell Nanoclusters, *J. Am. Chem. Soc.*, 2012, **134**(40), 16662–16670.

12 X. Ouyang, Y. Wu, Y. Gao, L. Li, L. Li, T. Liu, X. Jing, Y. Fu, J. Luo, G. Xie, S. Jia, M. Li, Q. Li, C. Fan and X. Liu, Micron-Scale Fabrication of Ultrathin Amorphous Copper Nanosheets Templated by DNA Scaffolds, *J. Am. Chem. Soc.*, 2023, **145**(8), 4553–4563.

13 L. Zanetti-Polzi, P. Charchar, I. Yarovsky and S. Corni, Origins of the pH-Responsive Photoluminescence of Peptide-Functionalized Au Nanoclusters, *ACS Nano*, 2022, **16**(12), 20129–20140.

14 X. Kang, Y. Li, M. Zhu and R. Jin, Atomically precise alloy nanoclusters: syntheses, structures, and properties, *Chem. Soc. Rev.*, 2020, **49**(17), 6443–6514.

15 X.-H. Ma, J.-T. Jia, P. Luo, Z.-Y. Wang, S.-Q. Zang and T. C. W. Mak, Layer-by-layer alloying of NIR-II emissive M50 (Au/Ag/Cu) superatomic nanocluster, *Nano Res.*, 2022, **15**(6), 5569–5574.

16 M. Kim, K. L. D. M. Weerawardene, W. Choi, S. M. Han, J. Paik, Y. Kim, M.-G. Choi, C. M. Aikens and D. Lee, Insights into the Metal-Exchange Synthesis of MAg24(SR) 18 (M = Ni, Pd, Pt) Nanoclusters, *Chem. Mater.*, 2020, **32**(23), 10216–10226.

17 Z.-H. Zhao, B.-L. Han, H.-F. Su, Q.-L. Guo, W.-X. Wang, J.-Q. Zhuo, Y.-N. Guo, J.-L. Liu, G.-G. Luo, P. Cui and D. Sun, Buckling cluster-based H-bonded icosahedral capsules and their propagation to a robust zeolite-like supramolecular framework, *Nat. Commun.*, 2024, **15**(1), 9401.

18 B. Huang and Y. Pei, On the mechanism of inter-cluster alloying reactions: two-stage metal exchange of $[Au_{25}(PET)_{18}]-$ and $[Ag_{25}(DMBT)_{18}]-$ clusters, *J. Mater. Chem. A*, 2020, **8**(20), 10242–10251.

19 A. Ghosh, O. F. Mohammed and O. M. Bakr, Atomic-Level Doping of Metal Clusters, *Acc. Chem. Res.*, 2018, **51**(12), 3094–3103.

20 C. Zhang, Z.-P. Yan, X.-Y. Dong, Z. Han, S. Li, T. Fu, Y.-Y. Zhu, Y.-X. Zheng, Y.-Y. Niu and S.-Q. Zang, Enantiomeric MOF Crystals Using Helical Channels as Palettes with Bright White Circularly Polarized Luminescence, *Adv. Mater.*, 2020, **32**(38), 2002914.

21 F. Zinna, U. Giovanella and L. D. Bari, Highly Circularly Polarized Electroluminescence from a Chiral Europium Complex, *Adv. Mater.*, 2015, **27**(10), 1791–1795.

22 Z. Zhang, J. Chen, X. Yan, X. Liu, Y. Chen, C. Zhao and L. Feng, One-step microwave preparation of carbon dots-composited G-quartet hydrogels with controllable chirality and circularly polarized luminescence, *Carbon*, 2023, **203**, 39–46.

23 F. Zinna and L. Di Bari, Lanthanide Circularly Polarized Luminescence: Bases and Applications, *Chirality*, 2015, **27**(1), 1–13.
24 Y. Yang, R. C. da Costa, M. J. Fuchter and A. J. Campbell, Circularly polarized light detection by a chiral organic semiconductor transistor, *Nat. Photonics*, 2013, **7**(8), 634–638.
25 S. Li, X.-Y. Dong, K.-S. Qi, S.-Q. Zang and T. C. W. Mak, Full-Color Tunable Circularly Polarized Luminescence Induced by the Crystal Defect from the Co-assembly of Chiral Silver(I) Clusters and Dyes, *J. Am. Chem. Soc.*, 2021, **143**(49), 20574–20578.
26 C.-L. Deng, B.-L. Han, Z.-Y. Liu, Z.-H. Pan, J. He, Y.-L. Li, Z.-L. Yang, G.-G. Luo, C.-H. Tung, D. Sun and L.-S. Zheng, Hierarchical Homochiral Assembly of Polyhedral Cage-Type Nanoclusters, *CCS Chem.*, 2024, **6**(10), 2537–2548.
27 G. Dong, Z. Pan, B. Han, Y. Tao, X. Chen, G.-G. Luo, P. Sun, C. Sun and D. Sun, Multi-layer 3D Chirality and Double-Helical Assembly in a Copper Nanocluster with a Triple-Helical Cu15 Core, *Angew. Chem., Int. Ed.*, 2023, **62**(24), e202302595.
28 J. Zhou, X. Yang, P. Zheng, Q. Li, X. Li, J. Chai, B. Huang, S. Yang and M. Zhu, Construction of an $Au_{12}Cd_2$ nanocluster with circularly polarized luminescence by a metal- and ligand-exchange strategy, *Chem. Sci.*, 2024, **15**(13), 4853–4859.
29 X. Wen, S. Du, L. Zhang and M. Liu, Chiral Deep Eutectic Solvents Enable Full-Color and White Circularly Polarized Luminescence from Achiral Luminophores, *Angew. Chem., Int. Ed.*, 2023, **62**(46), e202311816.
30 T.-Q. Yang, B. Peng, B.-Q. Shan, Y.-X. Zong, J.-G. Jiang, P. Wu and K. Zhang, Origin of the Photoluminescence of Metal Nanoclusters: From Metal-Centered Emission to Ligand-Centered Emission, *Nanomaterials*, 2020, **10**, 261.
31 T. Huang, L. Huang, W. He, X. Song, Z. Sun, Y. Jiang, G. Pan and S. Wei, Ammonia-Induced Size Convergence of Atomically Monodisperse Au_6 Nanoclusters, *J. Phys. Chem. C*, 2018, **122**(11), 6405–6411.
32 Z. Wu, Q. Yao, O. J. H. Chai, N. Ding, W. Xu, S. Zang and J. Xie, Unraveling the Impact of Gold(I)-Thiolate Motifs on the Aggregation-Induced Emission of Gold Nanoclusters, *Angew. Chem., Int. Ed.*, 2020, **59**(25), 9934–9939.
33 K. I. Hadjiivanov, D. A. Panayotov, M. Y. Mihaylov, E. Z. Ivanova, K. K. Chakarova, S. M. Andonova and N. L. Drenchev, Power of Infrared and Raman Spectroscopies to Characterize Metal-Organic Frameworks and Investigate Their Interaction with Guest Molecules, *Chem. Rev.*, 2021, **121**(3), 1286–1424.
34 Y. Ji, X. Yang, Z. Ji, L. Zhu, N. Ma, D. Chen, X. Jia, J. Tang and Y. Cao, DFT-Calculated IR Spectrum Amide I, II, and III Band Contributions of N-Methylacetamide Fine Components, *ACS Omega*, 2020, **5**(15), 8572–8578.
35 Y. Cai, F. Wang, Y. Hua, H. Liu, M. Yin, C. Zhang, Y. Zhang and H. Wang, A fluorimetric testing strip for the visual evaluation of mercury in blood using copper nanoclusters with DMSO-enhanced fluorescence and stability, *Nanoscale*, 2020, **12**(47), 24079–24084.
36 K. Pyo, V. D. Thanthirige, K. Kwak, P. Pandurangan, G. Ramakrishna and D. Lee, Ultrabright luminescence from gold nanoclusters: rigidifying the Au (I)-thiolate shell, *J. Am. Chem. Soc.*, 2015, **137**(25), 8244–8250.
37 Z. Wu, J. Liu, Y. Gao, H. Liu, T. Li, H. Zou, Z. Wang, K. Zhang, Y. Wang and H. Zhang, Assembly-induced enhancement of Cu nanoclusters luminescence with mechanochromic property, *J. Am. Chem. Soc.*, 2015, **137**(40), 12906–12913.
38 F. Neese, Software update: the ORCA program system, version 4.0, *WIREs Comput. Mol. Sci.*, 2018, **8**(1), e1327.
39 S. Roy, A. Baral, R. Bhattacharjee, B. Jana, A. Datta, S. Ghosh and A. Banerjee, Preparation of multi-coloured different sized fluorescent gold clusters from blue to NIR, structural analysis of the blue emitting Au7 cluster, and cell-imaging by the NIR gold cluster, *Nanoscale*, 2015, **7**(5), 1912–1920.
40 X. Zhu, Y. Li, P. Duan and M. Liu, Self-Assembled Ultralong Chiral Nanotubes and Tuning of Their Chirality Through the Mixing of Enantiomeric Components, *Chem.–Eur. J.*, 2010, **16**(27), 8034–8040.
41 S. Jia, B. Yang, Y. Xie, T. Tao, J. Du, L. Yu, Y. Zhang, J. Zhang, W. Tang and J. Gong, Dual-direction Circularly Polarized Luminescence Materials With On-demand Handedness and Superior Flexibility, *Adv. Funct. Mater.*, 2024, **34**, 2410206.
42 M. Lipok, P. Obstarczyk, S. Parzyszek, Y. Wang, M. Bagiński, T. Buergi, W. Lewandowski and J. Olesiak-Bańska, Circularly Polarized Luminescence from Atomically Precise Gold Nanoclusters Helically Assembled by Liquid-Crystal Template, *Adv. Opt. Mater.*, 2023, **11**(3), 2201984.